JOURNAL OF GEOPHYSICAL RESEARCH, VOL. 114, A03112, doi:10.1029/2008JA013888, 2009

On the common solar signal in different cosmogenic isotope data sets

Ilya G. Usoskin,[1] Kazuho Horiuchi,[2] Sami Solanki,[3] Gennady A. Kovaltsov,[4] and Edouard Bard[5]

Received 5 November 2008; revised 28 December 2008; accepted 3 February 2009; published 31 March 2009.

[1] In this article, we aim to determine frequency ranges and intervals of time in which the solar signal dominates in different cosmogenic isotope data. From a ^{14}C-based reconstruction of cosmic ray intensity over the last millennia, we computed expected ^{10}Be variations in two Antarctic sites (Dom Fuji and South Pole) and two Greenland sites (Dye-3 and GISP-2) and compared them with the actually measured ^{10}Be abundance at the sites. By applying different methods of analysis, such as bivariate correlation, conventional FFT coherence, and wavelet coherence, we found the following: (1) The modeled series, on the basis of ^{14}C data, are in good agreement with the measured ^{10}Be data sets, on different timescales and at different locations, confirming the existence of a common solar signal in both isotope data. (2) The ^{10}Be data are driven by the solar signal on timescales from about 100 years up to 1000 years or even to multimillennial scales (at the longer scales, paleomagnetism plays an increasingly important role). (3) The local climate dominates the ^{10}Be data mostly on short (<100 years) timescales, but the solar signal becomes important even at short scales during periods of Grand minima of solar activity. (4) There is an indication of a possible systematic uncertainty in the early Holocene, likely due to a not-perfectly-stable thermohaline circulation, which requires additional studies. We have shown that both ^{14}C- and ^{10}Be-based records are consistent with each other over a wide range of timescales and time intervals. They form a robust basis for quantitative reconstructions of solar activity variations in the past.

Citation: Usoskin, I. G., K. Horiuchi, S. Solanki, G. A. Kovaltsov, and E. Bard (2009), On the common solar signal in different cosmogenic isotope data sets, *J. Geophys. Res.*, *114*, A03112, doi:10.1029/2008JA013888.

1. Introduction

[2] While the 400-yearlong series of documented sunspot numbers forms one of the longest direct scientific records, it is important to obtain information on solar variations on even longer timescale. This allows essential observational constraints to be set upon the dynamo producing the Sun's magnetic field and, via the solar paradigm, also on cool sun-like stars. It is also vitally important for paleoclimatic and solar-terrestrial studies.

[3] The best known method to learn about solar variability in pretelescopic times is based on cosmogenic isotopes measured nowadays in stratified and independently dated archives, such as ^{10}Be in polar ice cores or ^{14}C in tree rings. Earlier studies were qualitative, based on linear regressions, but recent development of physics-based models has led to quantitative reconstructions [e.g., *Solanki et al.*, 2004; *Vonmoos et al.*, 2006]. Typically, only one data series is used to reconstruct the solar activity in the past, which does not allow the effect of possible violations of the underlying assumptions to be estimated. There was also an effort to superpose different ^{10}Be data sets into one composite series [*Muscheler et al.*, 2007], but the quality of such a synthetic series remains unclear [*Bard et al.*, 2007]. Visual comparisons of the results obtained from different isotope records [*Beer et al.*, 1988; *Bard et al.*, 1997; *Beer*, 2000; *Usoskin et al.*, 2003; *McCracken et al.*, 2004; *Vonmoos et al.*, 2006; *Horiuchi et al.*, 2008] generally confirm common variability in the ^{14}C and ^{10}Be isotopes, especially when applying some smoothing of the series. A comparison using cosmogenic ^{44}Ti measured in meteorites, a method which is not affected by terrestrial processes like climatic or geomagnetic field variability, has confirmed the overall agreement between different reconstructions over the last centuries [*Usoskin et al.*, 2006c]. However, even modern reconstructions remain indirect and based on different implicit and explicit assumptions (e.g., constant atmospheric and ocean ventilation, known paleomagnetic field variations, etc.), and the reliability and robustness of the reconstructions remains an important issue [*Dorman*, 2004].

[4] We note that the terrestrial fates of the two cosmogenic isotopes, ^{10}Be and ^{14}C, are dramatically different. Beryllium becomes attached to aerosols soon after its formation and thus is removed relatively quickly from the atmosphere.

[1] Sodankylä Geophysical Observatory, University of Oulu, Oulu, Finland.
[2] Faculty of Science and Technology, Hirosaki University, Hirosaki, Japan.
[3] Max-Planck Institute for Solar System Research, Katlenburg-Lindau, Germany.
[4] Ioffe Physical-Technical Institute, St. Petersburg, Russia.
[5] Collége de France, Université Paul-Cézanne Aix-Marseille, Europole de l'Arbois, Aix-en-Provence, France.

0148-0227/09/2008JA013888$09.00

Since the removal of ^{10}Be can be performed in different ways, the measured concentration in polar ice can be affected by climate/precipitation effects [e.g., *Lal*, 1987; *Steig et al.*, 1996; *Bard et al.*, 1997]. Many different processes may affect the isotope's concentration in polar ice, such as the fallout in the polar ice sheets which is partitioned differently between its wet and dry deposition and depends on local temperature, uneven (both spatially and temporally) stratosphere/troposphere mixing [*Lal and Lingenfelter*, 1991]. Some other uncertainties may be related to additional sources of ^{10}Be, such as aeolian dust [*Lal*, 2007] or solar energetic particle events [*Usoskin et al.*, 2006b]. These effects are nearly immediate due to the short residence time of ^{10}Be in the atmosphere. Thus ^{10}Be is sensitive to short-term climatic changes which affect meteorological parameters (atmospheric mixing and tropospheric scavenging). Although new sophisticated models of beryllium atmospheric transport are now appearing [*Field et al.*, 2006; *Heikkilä et al.*, 2008], the relation between production (solar) and deposition (local climate) signals in the ^{10}Be is still not fully resolved [*Dorman*, 2004; *Pedro et al.*, 2006; *Belmaker et al.*, 2008].

[5] Radiocarbon ^{14}C is oxidized to CO_2 and therefore takes part, in gaseous form, in the global carbon cycle and can be eventually stored in a tree where the year of its deposition can be determined via dendrochronology. The carbon cycle has a complicated frequency-dependent response to the variations of the ^{14}C production [see, e.g., *Siegenthaler et al.*, 1980]. Radiocarbon is assumed to be globally mixed in the atmosphere before being trapped by a living tree. The most important parameter for the ^{14}C concentration in the system is the pace of ocean ventilation [e.g., *Kromer et al.*, 2001; *Hughen et al.*, 2004]. It is usually assumed constant for the Holocene [*Damon et al.*, 1978; *Stuiver et al.*, 1991; *Gerber et al.*, 2002]. Accordingly all variations of the Δ^{14}C (the measure of ^{14}C relative activity, see study by *Stuiver and Pollach* [1977]) are thought to predominantly reflect the production rate. On the other hand, the changing climate and in particular ocean ventilation prevents quantitative studies of solar variability before the Holocene, i.e., during earlier ice age and deglaciation periods, because of the extended dependence of the carbon cycle to the previous conditions. Note that some chances in the thermohaline circulation might have occurred even during the Holocene [*Oppo et al.*, 2003; *Ellison et al.*, 2006; *Kleiven et al.*, 2008], but the present knowledge does not allow to perform an accurate modeling of the effect. These terrestrial changes affecting the ^{14}C content are rather slow and delayed. Therefore the two isotopes are differently affected by terrestrial conditions on different timescales and thus any common variability can be at least largely ascribed to extraterrestrial (solar) drivers.

[6] Several studies comparing records of ^{10}Be and ^{14}C isotopes have been performed. Of special interest is a thorough study by *Bard et al.* [1997]. They assumed that ^{10}Be concentration measured in an ice core from the South Pole reflects only the solar signal, and applied it as input for the ^{14}C production and the carbon cycle model, which was then confronted with the actually measured Δ^{14}C in tree rings, for the period 850–1900 AD. The similarity between the actual and ^{10}Be-based radiocarbon series implies that both isotopes mostly reflect solar variability on the inter-centennial timescale. A recent comparison of solar activity reconstructions from ^{10}Be GISP series and from the ^{14}C series [*Vonmoos et al.*, 2006] has shown that, while the agreement between them is good on a centennial-millennial timescale, a significant discrepancy is observed in the multi-millennial trend, whose nature is unclear. We note that the earlier studies were based on only one ^{10}Be series in each case, and were limited to simple correlations. Thus they did not analyze evolution of the common solar signal in the time and/or frequency domains.

[7] In this paper we further develop this type of analysis, systematically using all isotope series available to us and extending the study into the frequency (FFT coherence) and time/frequency domains (wavelet coherence). We choose a scheme opposite to that of *Bard et al.* [1997], viz. we start from the ^{14}C-based reconstruction of cosmic ray intensity and compare the expected ^{10}Be variations with those measured at four polar sites. This choice is based on the following reasons. The ^{14}C variations represent the global signal and are less prone to the local effects since the benchmark Δ^{14}C series is a result of an international collaboration [*Stuiver et al.*, 1998; *Reimer et al.*, 2004] of measurements of samples distributed over the Globe. Moreover, a recent physics-based model allows absolute reconstruction of the cosmic ray flux and solar activity in the past [*Solanki et al.*, 2004]. In contrast, all ^{10}Be series are local and may be influenced by the polar meteorology [*Lal*, 1987; *Beer et al.*, 1990]. In addition, a quantitative link connecting the measured concentration and cosmic ray-induced production of ^{10}Be is still missing. Therefore we decided to start from the ^{14}C data and compute consequently the cosmic ray flux variations and then the expected ^{10}Be series for each of the polar sites separately, as described in section 2.2.

[8] Applying different methods, we perform a systematic analysis aiming to find frequency and time ranges where the solar signal dominates over terrestrial processes. In section 2 we describe the data and methods upon which we base our analysis (some technical details are given in two Appendices), section 3 presents the results separately for the bivariate correlation, FFT coherence and wavelet coherence analyses as well as providing a summary of the results. Conclusions are presented in section 4.

2. Measured and Computed Data Sets

2.1. Measured Series of ^{10}Be in Polar Ice

[9] Here we analyze four data sets of ^{10}Be measurements in polar ice cores (see Figure 1). The main parameters of the series are given below and summarized in the first block of Table 1. Two series are from Antarctica and two from Greenland, thus being from nearly antipodal sites. Even the nearest station pairs are separated by 1000–1500 km. This excludes (for antipodal sites) or minimizes (for nearby sites) the common local climate effect, so that the coherent variations can be ascribed to the ^{10}Be production or, to a lesser extent because of the stable Holocene climate, to the global climate variability.

[10] All series has been converted into decadal time resolution to suppress the 11-year cycle and to be directly comparable with the modeled series (section 2.2). The ^{10}Be data is usually given either as concentration (atoms per

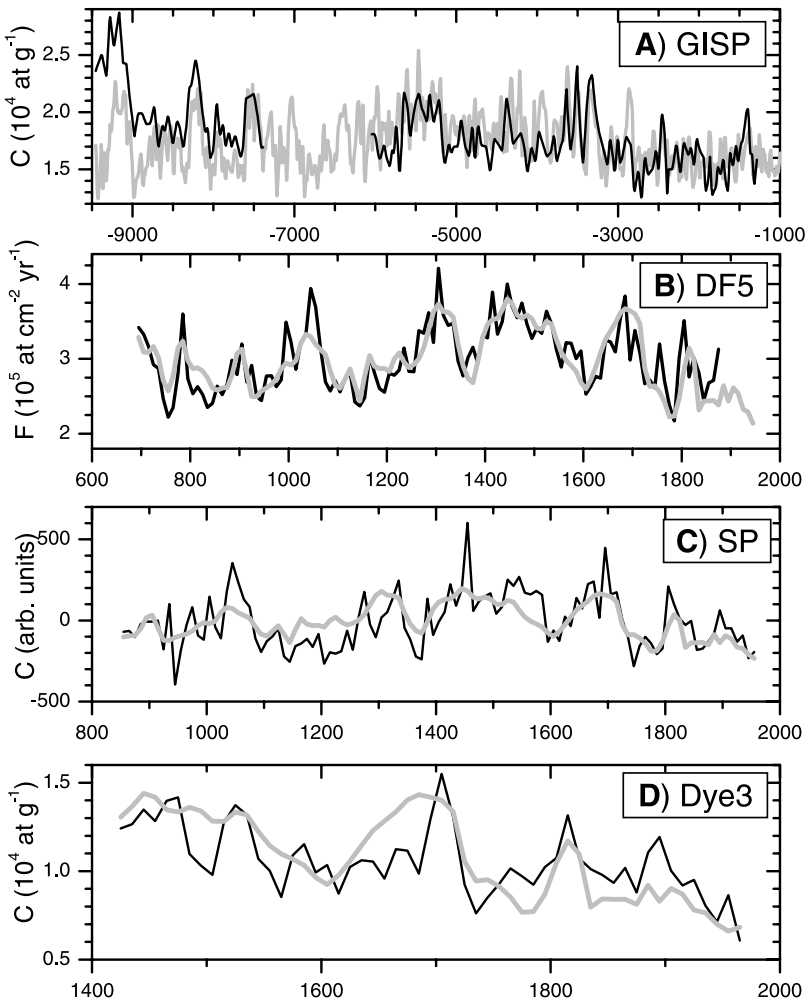

Figure 1. Measured (solid curves) and modeled (gray curves) ^{10}Be data, see text for details. (a) *GISP*-2 series and *Y*00(*M*) model. (b) Dome Fuji *DF*5 series and *AI*(*M*) model. (c) South Pole *SP* series and *AI*(*M*) model. (d) *Dye*-3 series and *AI*(*M*) model. Note the different timescales.

gram of ice) or flux (atoms deposited per cm^2 per year). The two quantities are related via the snow accumulation rate. Although the accumulation rate may change by a factor of 2 between warm periods and glacial times, it can be assumed nearly constant during the Holocene [e.g., *Beer*, 2000]. The four series cover different periods of time, from 600 years (*Dye*-3 series) to several millennia for the *GISP* series. In order to be on the safe side, we discarded the data after

Table 1. Data Sets and Models Used in This Study

Model/Data Set	Time Span	Parameters
	Data Sets	
Dome Fuji (*DF*5) [*Horiuchi et al.*, 2008]	690–1880 AD	Antarctica (77.3°S 39.7°E), flux
South Pole (*SP*) [*Bard et al.*, 1997]	850–1950 AD	Antarctica (South Pole), concentration, relative units
Dye-3 [*Beer et al.*, 1990]	1424–1950 AD	Greenland (65.2°N 43.8°W), concentration
GISP-2 [*Finkel and Nishiizumi*, 1997]	9500–1320 BC[a]	Greenland (72.6°N 38.5°W), concentration
	Paleomagnetic Models	
ArcheoInt (*AI*) [*Genevey et al.*, 2008]	1000 BC–2000 AD	realistic shifted dipole approximation used
CALS7K.2 (*CALS*) [*Korte and Constable*, 2006, 2008]	5000 BC–2000 AD	realistic shifted dipole approximation used
Yang et al. [2000] model (*Y*00)	9500 BC–2000 AD	only VADM available, no directional information
	Atmospheric Mixing Models	
Polar (*P*) model	–	troposphere 60–90°, stratosphere 60–90°
Medium (*M*) model	–	troposphere 60–90°, stratosphere 0–90°
Global (*G*) model	–	troposphere 0–90°, stratosphere 0–90°

[a]There is a data gap, circa 7450–6050 BC.

1950 AD since the uppermost snow/firn layers can be affected by exchange with the atmosphere [e.g., *Lal et al.*, 2001].

[11] The Antarctic Dome Fuji series [*Horiuchi et al.*, 2007, 2008], denoted henceforth as *DF*5 (see Table 1) provides the ^{10}Be deposition flux obtained from ^{10}Be concentration in ice as well as the snow accumulation rate, which was estimated from δ^{18}O. In order to minimize the influence of random noise, the snow accumulation rate was calculated from five running average δ^{18}O data points. The *DF*5 series, covering the period 690–1880 AD, is shown in Figure 1b.

[12] The Antarctic *South Pole SP* series provides relative variations of ^{10}Be concentration (in per mille) at the South Pole site [*Bard et al.*, 1997] starting circa 850 AD, and we consider the period 850–1950 AD.

[13] The *Dye*-3 series represents measurements of ^{10}Be concentration (in atoms per gram of ice) in Greenland [*Beer et al.*, 1990], starting 1424, and we consider the period 1420–1950 AD.

[14] The *GISP* series represents measurements of ^{10}Be at the Greenland Ice Sheet Project 2 (GISP-2) site in Greenland [*Finkel and Nishiizumi*, 1997]. The series covers the period from about 9500 BC to 1320 BC but contains a gap between 7450 BC and 6050 BC (Figure 1a). Note that the *GISP* series does not overlap with the other three ^{10}Be series.

2.2. ^{14}C-Based Series of ^{10}Be

[15] Here we describe a model to compute the ^{10}Be production from ^{14}C data. The model consists of several steps, as described in detail below.

[16] First, using a prescribed paleomagnetic model, temporal variations of the cosmic ray (CR) flux are computed from ^{14}C data. Subsequently, from thus computed cosmic ray flux variations, the ^{10}Be production in the atmosphere is calculated for a prescribed paleomagnetic model and atmospheric mixing model. A scheme of the approach is as follows:

$$\Delta^{14}\mathrm{C} \xrightarrow{(1)} Q_{14\mathrm{C}} \xrightarrow{(2)} \text{CR flux} \xrightarrow{(3)} Q_{10\mathrm{Be}} \xrightarrow{(4)} C_{10\mathrm{Be}}. \qquad (1)$$

[17] Step (1) includes computation of the global production rate of ^{14}C from the measured radiocarbon activity Δ^{14}C. As the basis we use the INTCAL Δ^{14}C data set representing the global absolutely dated series of Δ^{14}C for the period 23,000 BC–1950 AD measured in tree rings over the world [*Stuiver et al.*, 1998; *Reimer et al.*, 2004]. We have adopted the ^{14}C production rate Q_{14C} computed by *Usoskin and Kromer* [2005] from the measured INTCAL Δ^{14}C series using the global carbon cycle model. Because of the Suess effect [*Suess*, 1955; *Tans et al.*, 1979] of dilution of the atmospheric $^{14}CO_2$ concentration because of extensive fossil fuel burning ^{14}C data can be used only till 1900. After that we used the CR flux computed from the sunspot-based reconstruction of the solar open magnetic flux [*Usoskin et al.*, 2004; *Krivova et al.*, 2007]. We note that, since the ^{14}C data represents the global production, this conversion is sensitive not to the atmospheric circulation but mostly to the ocean ventilation, which is assumed here to be fairly constant throughout the Holocene. Therefore the carbon cycle has been considered steady state corresponding to the preindustrial epoch [*Siegenthaler et al.*, 1980], which may however, introduce systematic uncertainties (bias) in the earlier part of the Holocene (see section 3.4).

[18] Step (2) includes computation of the time-variable cosmic ray flux from Q_{14C} using a prescribed paleomagnetic model (section 2.3). Variations of the cosmic ray flux due to heliospheric modulation is the main driver of the solar signal in cosmogenic isotope data [e.g., *Beer*, 2000]. The cosmic ray flux can be well parameterized using the so-called modulation potential ϕ, which adequately describes the energy spectrum of cosmic rays in a wide range of parameters (see the related formalism and definitions in the study by *Usoskin et al.* [2005]). In order to calculate the corresponding variations of the cosmic ray flux in terms of the modulation potential ϕ we use the methods of *Solanki et al.* [2004] and *Usoskin et al.* [2004, 2007]. Cosmic ray flux variations after 1610 were calculated through the solar open magnetic flux reconstructions [*Usoskin et al.*, 2002]. The conversion between Q_{14C} and ϕ depends strongly on the applied paleomagnetic model [*Usoskin et al.*, 2006a; *Snowball and Muscheler*, 2007]. Therefore we have computed the series of the modulation potential ϕ separately for each paleomagnetic model used, as described in the next subsection.

[19] Once the cosmic ray flux, quantified via the modulation potential ϕ, and the paleomagnetic model are fixed, we can proceed to step (3) and compute the production rate $Q_{10\mathrm{Be}}$ of ^{10}Be in the atmosphere as a function of geographical location (actually the local geomagnetic cutoff rigidity P_c) and altitude h as

$$Q_{10\mathrm{Be}}(h, P_c, \phi) = \int_{E_c}^{\infty} Y_{10\mathrm{Be}}(E, h) \cdot S(E, \phi) \cdot dE, \qquad (2)$$

where $Y_{10\mathrm{Be}}$ is the yield function of ^{10}Be production, S is the differential energy spectrum of cosmic rays, and integration is over the kinetic energy of cosmic rays E above E_c which corresponds to the cutoff rigidity P_c. Calculations were done using the cosmic ray spectrum parameterized by *Usoskin et al.* [2005], and the yield function of Beryllium production by cosmic rays in the atmosphere [*Usoskin and Kovaltsov*, 2008]. A full three-dimensional (geographical × altitude) grid of the isotope's production have been calculated for each time step using the prescribed values of $\phi(t)$ and $P_c(t)$ (calculated within a given paleomagnetic model).

[20] We can finally go to step (4) and calculate the ^{10}Be data, as a spatial average of the three-dimensional production rate (the result of step (3)) in the region defined by the atmospheric mixing model (section 2.4). The measured values are then assumed proportional to thus defined integral production. We note that we do not require any absolute normalization of the computed ^{10}Be data, since relative variations are enough for the subsequent correlation/coherence analysis.

2.3. Paleomagnetic Models

[21] Because of additional shielding provided by the geomagnetic field against cosmic rays, the relation between the CR flux at the Earth's orbit and cosmogenic isotope production rate depends on the exact geomagnetic field strength. This is probably the largest uncertainty in the

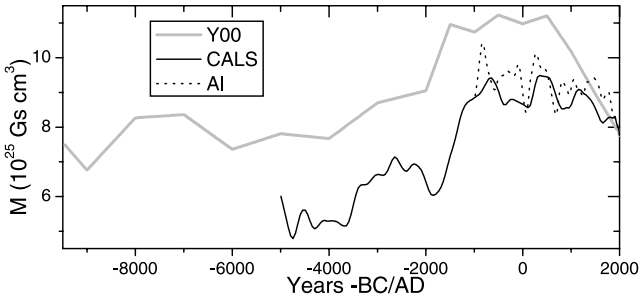

Figure 2. Geomagnetic dipole moment M reconstructions according to different paleomagnetic models (see Table 1 and section 2.3).

reconstructed solar activity [*Solanki et al.*, 2004; *Snowball and Muscheler*, 2007]. Variations of the geomagnetic field in the past are evaluated independently by paleomagnetic and/or archeomagnetic methods of reconstruction and form paleomagnetic models. Most important for the cosmic ray shielding is the dipole moment of the geomagnetic field, which provides global shielding. However, when considering regional effects, especially for the ^{10}Be transport, one also needs directional information of the geomagnetic field, since wandering of the dipole axis may strongly affect the geomagnetic cutoff and thus the local CR flux at mid-latitude to high-latitude regions on centennial timescales [*McCracken*, 2004; *Usoskin et al.*, 2008].

[22] Here we consider three paleomagnetic models (see second block in Table 1) which extend back over different lengths of time, as depicted in Figure 2. All the models yield a similar pattern of enhanced magnetic field 1–3 millennia ago, compared to other periods, but the fine details and the absolute value of the magnetic moment are different.

[23] The longest model *Y*00 [*Yang et al.*, 2000] covers the whole Holocene but provides only the virtual axial dipole moment (VADM), i.e., assumes that the dipole field is aligned with the geographical axis. The directional information of the dipole axis is not available. The *CALS*7K2 model [*Korte and Constable*, 2006, 2008] provides reconstructions of both the true dipole moment and the geomagnetic axis direction for the last 7000 years. We note that the VADM may differ significantly from the true dipole moment, mostly overestimating it by assigning nondipole contributions to the dipole strength (see, e.g., discussions by *McMillan et al.* [2004] and *Korte and Constable* [2005]). On the other hand, the *CALS*7K2 model may slightly underestimate the dipole moment by ascribing too much power to the higher momenta.

[24] The *AI* model is a recent paleomagnetic reconstruction for the last 3000 years performed by an international collaboration ArcheoInt [*Genevey et al.*, 2008]. The *AI* model provides both the dipole moment and the directional information and includes all the presently available paleomagnetic data sets. Accordingly, we will base our results mostly on the *AI* model for the last millennium.

[25] In order to represent the geomagnetic field for the 20th century we use the IGRF (International Geomagnetic Reference Field, see, e.g., the study by *MacMillan and Maus* [2005]) model. When computing the ^{10}Be production rate at a given location, we take into account both the dipole moment and the direction of the slowly migrating magnetic axis for all the paleomagnetic models except for the *Y*00 one, for which the magnetic axis is considered to be permanently aligned with the geographical axis. For *AI*, *CALS* and *IGRF* models we used an approximation of the eccentric dipole which provides a good compromise between simplicity and reality [*Fraser-Smith*, 1987]. The eccentric dipole has the same dipole moment and orientation as the centered dipole, but the dipole's center is shifted with respect to the geographical one. For the *Y*00 model, only centered dipole aligned with the geographical axis can be estimated.

2.4. Atmospheric Mixing Models

[26] Soon after production in the atmosphere ^{10}Be atoms become attached to aerosols and follow their fate. Generally, the residence time of ^{10}Be in the troposphere is short, several weeks, because of the fast scavenging and wash out. However, it may reach a few years in the stratosphere [e.g., *Beer*, 2000]. The situation is further complicated by seasonal breakthroughs of stratospheric air into the troposphere. Because of the short residence time, ^{10}Be is not necessarily globally mixed before deposition, contrary to ^{14}C, thus the measured concentration can represent production in a limited geographical area. Detailed models of Beryllium transport in the atmosphere, based on general circulation models, are currently being developed [*Field et al.*, 2006; *Heikkilä et al.*, 2008], which are generally consistent with the observations. However, the problem is not yet resolved to the extent that it allows for a quantitative conversion between the ^{10}Be production rate and measured concentration/flux in ice, especially in the past. Accordingly it is common to assume that the measured concentration is directly proportional to the production in a limited geographical region as prescribed by an ad hoc atmospheric mixing model [see, e.g., discussion by *McCracken*, 2004]. Here we consider three mixing models (see third block in Table 1).

[27] One mixing model, denoted as the polar (*P*) model, assumes that the ^{10}Be measured in polar ice reflects only polar production, above 60° latitude. This corresponds to the mixing model M1 by *McCracken* [2004] as well as to the assumptions used by *Bard et al.* [1997] and *Usoskin et al.* [2003].

[28] The global (*G*) mixing model assumes that ^{10}Be is totally mixed in the hemispheric atmosphere before deposition in polar regions, without exchange between the Northern and Southern hemispheres though. This model corresponds to the assumptions made by *Beer* [2000] and to the M6 model by *McCracken* [2004].

[29] The two above mixing models, *P* and *G*, bounds the possible range of limited mixing. We have considered also the medium (*M*) model, where the polar deposition corresponds to the hemispherically mixed stratosphere, but to only the polar (above 60° latitude) troposphere. As a boundary between troposphere and stratospheres we used the mean realistic latitude-dependent height of the tropopause as defined by the World Meteorological Organization. This model is close to the assumptions made by *Vonmoos et al.* [2006] and to the M4 model by *McCracken* [2004].

[30] We note that the difference between the mixing models becomes significant mostly on long timescales. In

Table 2. Coefficients (Together With 1σ Uncertainties) of Cross-Correlation Between Different ^{10}Be Series Studied in the Paper[a]

	Dye-3	*SP*	*DF*5	*GISP*	*G* versus *P* [b]
		Block I			
SP	0.48 ± 0.2	1			
*DF*5	$0.57^{+0.17}_{-0.23}$	$0.57^{+0.12}_{-0.15}$	1		
		Block II			
AI(*M*)	$0.71^{+0.11}_{-0.16}$	$0.72^{+0.08}_{-0.10}$	$0.72^{+0.11}_{-0.15}$	N/A[c]	0.92 ± 0.02
CALS(*M*)	$0.71^{+0.11}_{-0.16}$	$0.70^{+0.08}_{-0.11}$	$0.76^{+0.07}_{-0.09}$	$0.60^{+0.06}_{-0.07}$	$0.63^{+0.04}_{-0.05}$
*Y*00(*M*)	$0.73^{+0.10}_{-0.15}$	$0.70^{+0.08}_{-0.11}$	$0.78^{+0.06}_{-0.06}$	$0.51^{+0.06}_{-0.06}$	0.82 ± 0.02

[a]For description of the series, see text.
[b]Correlation between series computed using the fixed geomagnetic model but different *G* and *P* mixing models (see text).
[c]Time series do not overlap.

this paper we perform most calculations using the medium (*M*) mixing model and discuss the effects of the other two models, *G* and *P*.

3. Results of Comparison

[31] Here we present a comparison between the actually measured and the ^{14}C-based series, computed in section 2, of ^{10}Be on different time/period scales. The calculated ^{10}Be series are denoted henceforth as *XXX*(*Y*), where *XXX* stands for the paleomagnetic model, and *Y* denotes the atmospheric mixing model. For example, the *AI*(*M*) series denotes the ^{10}Be series computed from ^{14}C using the ArceoInt paleomagnetic model and the medium mixing model.

[32] A visual comparison between the measured and corresponding computed-from-^{14}C ^{10}Be series is shown in Figure 1, showing a good agreement between them. In the following we study the agreement in further detail using different quantitative tests.

3.1. Bivariate Correlation

[33] The first and simplest index of an agreement between relative variations of two time series *X* and *Y* is the bivariate (Pearson's) correlation r_{xy}. It quantifies in one number the overall correlation between the two entire series on all timescales. The correlation coefficients are given in Table 2 for all pairs of the analyzed series.

[34] Block I presents correlations between the actually measured ^{10}Be time series. The series demonstrate highly significant (better than $2\ 10^{-4}$) correlation, which is widely considered as evidence of their common (solar) origin. However, the correlation coefficients are not very high, being $r = 0.48-0.57$, suggesting that the series contain also essential components (local climate or noise), which are individual for each series.

[35] Block II of Table 2 presents correlations between the measured and computed series. All the correlations are highly significant (the probability of a random occurrence of such a correlation is lower than 10^{-9}). The correlation coefficients are above 0.7 for all the studied series, except for the long GISP series, and are higher than the correlation between individual measured series (see Block I in Table 2). This suggests that indeed the individual ^{10}Be series are more noisy, likely due to the local climatic variability that may affect the short-term variations of ^{10}Be, than the computed series based on the global ^{14}C data. This level of correlation (about 0.7) is consistent with the correlation between ^{14}C and 10-year lagged South Pole ^{10}Be series found by *Bard et al.* [1997]. We note that our approach does not require any lag between the series since the carbon cycle, responsible for the measured ^{14}C signal lagging behind ^{10}Be, is explicitly taken into account (section 2.2). Although the correlation coefficient is lower (0.51) for the long *GISP* series, its significance remains very high (10^{-20}) because of the series' length.

[36] Correlations between all the computed series based on different paleomagnetic but fixed mixing models are very high, $r \geq 0.99$. This is basically due to the fact that the correlation coefficient is dominated by the short-term variations in the time series whereas the geomagnetic series mainly influence the long-term trend. When the paleomagnetic model is fixed, but the atmospheric mixing model changes between global (*G*) and polar (*P*) models, the correlation coefficient between the computed series varies (see Table 2, column 6). It is high for the short AI and long but dipole aligned *Y*00 paleomagnetic models and somewhat lower for the 7000 years long and realistic dipole *CALS* model, mostly because of the effect of wandering of the geomagnetic axis. The correlation between (*M*) and either (*P*) or (*G*) models is always above 0.9.

[37] Correlation coefficients alone do not allow to study the details of the relation between the series.

3.2. FFT Coherence

[38] Next we study the FFT coherence between the series, which is defined as the normalized cross-spectrum in the frequency domain. We used the standard magnitude-squared coherence [*Kay*, 1988], $C_{xy}(f)$, which quantifies (between 0 and 1 corresponding to no coherence and perfect coherence, respectively) the agreement between two series *x* and *y* at frequency *f*:

$$C_{\mathrm{xy}}(f) = \frac{|S_{\mathrm{xy}}(f)|^2}{S_{\mathrm{xx}}(f) \cdot S_{\mathrm{yy}}(f)}, \tag{3}$$

where *S* stands for the power spectral density of either the cross spectrum *xy* or the individual series *x* or *y*. This coherence can be interpreted as localization of the correlation coefficient in the frequency domain, so that correlation is shown as a function of frequency/period, averaged over the entire time interval. FFT coherence plots of selected pairs of time series are shown in Figure 3.

[39] First we tested the coherence between modeled series produced using different atmosphere mixing models. As an

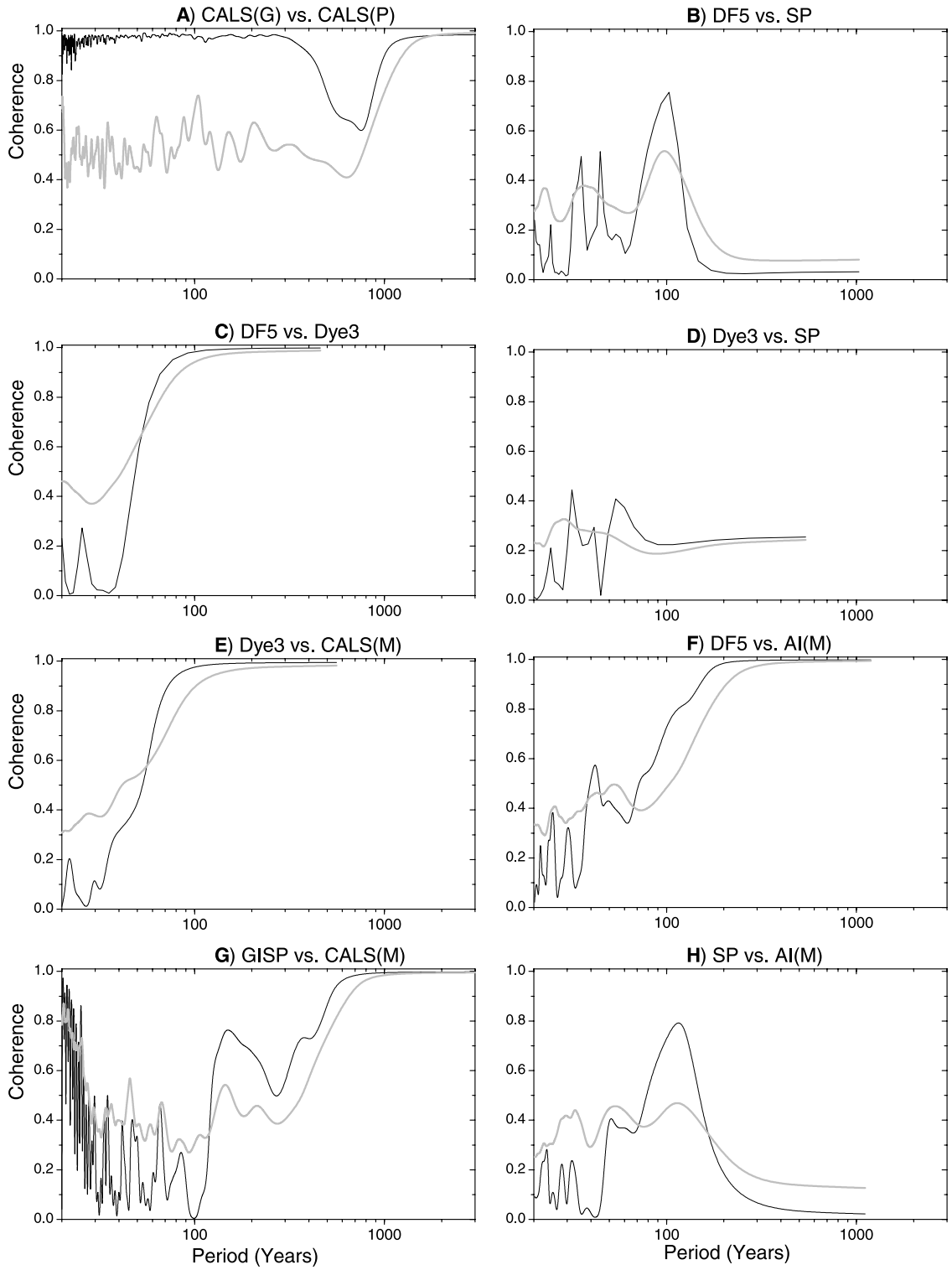

Figure 3. FFT coherence (solid curves) between different analyzed series as indicated in the top of each panel. Gray curves correspond to the 95% confidence level estimated using a nonparametric random phase test (see Appendix A).

example, the FFT coherence between *CALS*(*G*) and *CALS*(*P*) is shown in Figure 3a. One can see that the coherence is very high (above 0.95) at all the periods except for the range between circa 200 and 1000 years. This can be understood as separation of different effects: on timescales shorter than 200 years the variability is mostly defined by solar modulation which is the same for both series, while changes of the geomagnetic dipole moment are important on multimillennia timescales. On the centennial timescale, however, the wandering of the geomagnetic axis is important for the polar but not for the global mixing model,

leading to a reduced coherence. Note that the coherence is highly significant (better than 0.05) for all periods.

[40] Next block (Figures 3b–3d) shows the coherence between the measured ^{10}Be series. The coherence between *Dye*-3 and *DF*5 series is high for the periods above 60 years (panel c). On the other hand, the coherence is not high between the *SP* series and either *Dye*-3 (panel d) or *DF*5 (panel b) series. It is significant (at the 0.05 level) only in the range of periods around hundred years. Of particular interest is the lack of coherence between the two Antarctic series, *DF*5 and *SP*. However, as discussed in the next subsection, this mismatch is seeming.

[41] Coherence between the modeled and measured series (panels e–h) is high and significant for periods above 60–100 years in most cases. The only exception is the *SP* series, which depicts a high coherence with all other measured or modeled series considered here only around the 100-year timescale.

3.3. Wavelet Coherence

[42] The wavelet coherence is, similar to the FFT coherence, defined as the normalized wavelet cross-spectrum

$$WC_{xy}(f,t) = \frac{|W_{xy}(f,t)|^2}{W_{xx}(f,t)\cdot W_{yy}(f,t)}, \qquad (4)$$

where W stands for the wavelet spectral density localized at frequency f and time t. Wavelet coherence determines both the absolute magnitude, defined between 0 (no coherence) and 1 (100% coherence), and the phase shift between the series, as a function of the frequency/timescale and time. The wavelet coherence can be regarded as further localization of the FFT coherence. Whereas the latter is defined only in the frequency domains, the wavelet coherence reveals locations in both time and frequency where the coherence is large.

[43] Here we apply the commonly used Morlet basis for the wavelet spectra with the damping parameter (or dimensionless time η [e.g., *Grinsted et al.*, 2004]) equal to 3, which provides better time resolution (in particular reducing the cone of influence) at the cost of a lower frequency resolution. We note that for the selected parameters, the timescale (i.e., effective expansion of a wavelet package in the time domain) is close to the nominal Fourier period (i.e., inverted carrier frequency of the Morlet function). Therefore we will use the term ''timescale'' throughout the paper.

[44] The wavelet coherence plots are shown in Figure 4, with the panels corresponding to those in Figure 3. Colors corresponds to the magnitude of the coherence (from blue to red). We consider here also the relative phasing between the analyzed series. In cases when the local phase mismatch between the series (i.e., the relative phase shift needed to obtained the highest coherence at the given frequency and time) exceeds the conservative limit, defined in Appendix B, the coherence is discarded irrespective of its magnitude. Areas in the coherence plots, corresponding to such phase mismatch, are filled in white. The statistical significance of the wavelet coherence was estimated using the nonparametric random phase test (see Appendix A). Hatched areas denote the so-called cone of influence (COI), which indicate that the results can be affected by the edges of the series and thus are not reliable inside these areas. Strictly speaking, the areas within the COI need to be discarded.

[45] In agreement with the FFT coherence, the wavelet coherence between the *CALS*(G) and *CALS*(P) series (panel a) is very high for all timescales shorter than 500–600 years. For longer timescales, not only the coherence becomes lower but also the phase mismatch between the two modeled series becomes too high, because of the influence of the geomagnetic pole migration on the *CALS*(P) series. For timescales longer than 3000–4000 years, the series again become coherent (see Figure 3). Thus the coherence pattern between the global and polar mixing models of ^{10}Be production are essentially similar when using FFT or wavelet coherences. The situation, however, is more complicated for directly measured time series, where the use of wavelet coherence allows details to be studied that are not available to the FFT coherence method.

[46] While the FFT coherence between the *SP* and *DF*5 series is significant at around the 100-year period only (Figure 3b), the wavelet coherence between the same series (Figure 4b) is dominated by the high coherence (red color) everywhere for timescales longer than 80–100 years. This seeming discrepancy can be explained when the phasing between the series is considered. An example of the relative phase shift between the two series is shown in Figure 5 at the nominal period of 268 years, where the FFT coherence is close to zero but the wavelet coherence is high. One can see that the phase difference between the series, at this frequency, varies essentially between $-\pi/2$ and almost $\pi/2$, implying that the series may be offset by up to 50–60 years in both directions. We note that the modeled and measured data sets are based on different methods of dating [e.g., *Kromer and Spurk*, 1998]. The absolute dating of ^{10}Be data contains some uncertainties which can range from a few years for the last centennia up to several decades in the early Holocene [e.g., *Raisbeck et al.*, 1990; *Vinther et al.*, 2006; *Horiuchi et al.*, 2007]. Accordingly, the FFT method cannot find a sensible match between the series in the entire 1000-year long interval. On the other hand, the wavelet method finds a perfect coherence within the timescale with variable phase shift. Accordingly, contrary to the FFT result suggesting the lack of coherence between *SP* and *DF*5 series for periods exceeding roughly 200 years, the wavelet approach finds a very high coherence, in the entire range of timescales (above 80–100 years) and times outside COI, with the variable but within the conservative limit phase shift. It is interesting that the coherence extends to shorter scales (to about 50 years) during an interval between 1000 and 1150 AD. We note that this interval is characterized by a rapid variability of the solar activity between a Grand minimum around 1050 AD and relatively high activity circa 1200 AD [*Usoskin et al.*, 2007]. Another spot of high coherence at high frequency is observed circa 1800 AD, i.e., around the Dalton minimum.

[47] The coherence between *DF*5 and *Dye*-3 series (panel c) is characterized by a large area of high coherence, covering almost the entire range (outside the COI) of timescales longer than 100–150 years and two smaller spots of coherence at shorter timescales around 1500–1600 AD and circa 1800 AD (i.e., during the Spörer and Dalton minima, respectively). While being in general agreement with the FFT coherence (Figure 3c), this result reveals a more interesting pattern.

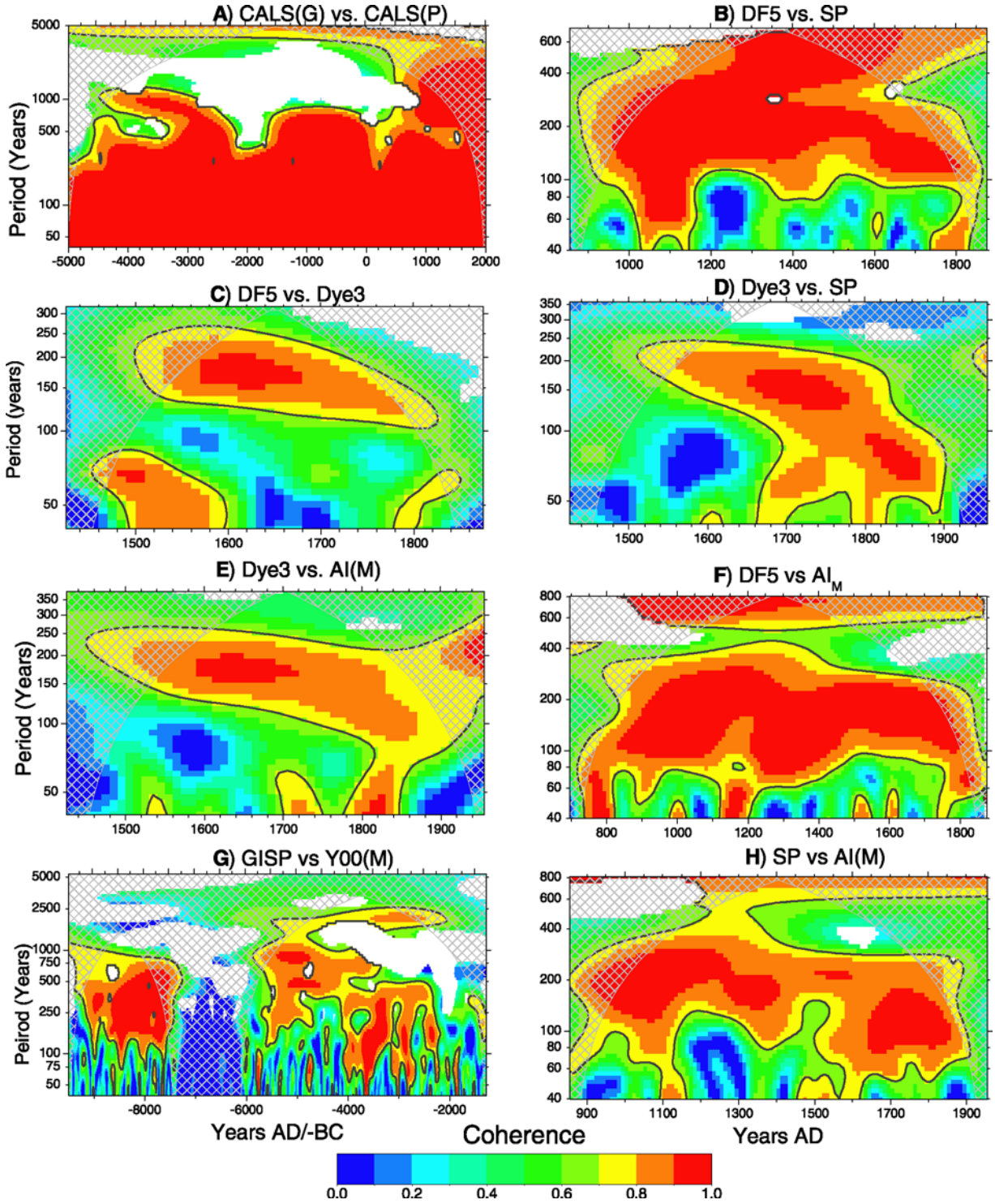

Figure 4. Wavelet coherence between analyzed series as indicated above each panel (color scale at the bottom of the figure). Black curves bound the 95% confidence level estimated using a nonparametric random phase test (see Appendix A). White areas correspond to significant phase mismatch between the series (see Appendix B). Gray-hatched areas denote the cone of influence (COI) where the result is unreliable.

[48] The *Dye*-3 and *SP* series (panel d) are cross-coherent in the range of timescales between 100–150 and 250 years with the area of high coherence extending to shorter scales in the second half of the analyzed time interval, down to 40 years, during the Maunder (circa 1700) and Dalton (circa 1800) minima of solar activity. Just as for panel b, a seeming discrepancy between the FFT and wavelet coherence patterns can be explained by the relative phasing.

[49] The coherence between the *Dye*-3 and *AI*(*M*) series (panel e) also displays a similar pattern: the main domain of

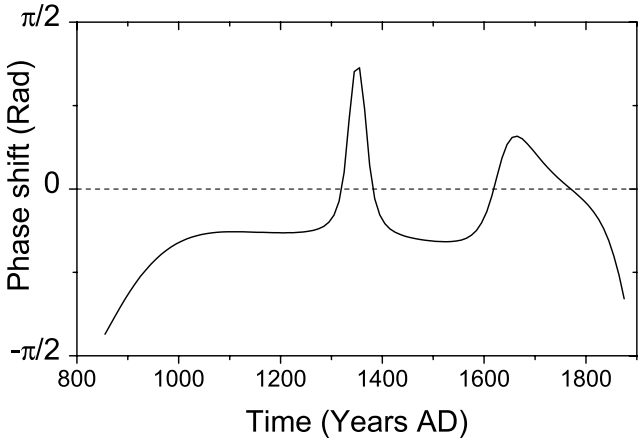

Figure 5. Time profile of the phase shift between the *SP* and *DF*5 series, computed from the wavelet coherence at period 268 years.

high coherence, which covers timescales between 120 and 250 years in the early part of the time interval, later expands toward shorter scales (about 70 years). Spots of enhanced coherence at circa 1800, 1700 and circa 1540 (this last being very small), corresponding to the Dalton, Maunder and Spörer minima, can be noticed.

[50] The coherence between *DF*5 and *AI*(*M*) series (panel f) is high for all timescales between 80–100 years and 300 years and above 500 years. Note that the coherence gap at 300–500 years is greatly reduced if *AI*(*G*) series is used instead of the *AI*(*M*) series. Yet all the expansions of regions of high coherence to shorter scales correspond to Grand minima of solar activity.

[51] Panel g presents coherence between the *GISP* and *Y*00(*M*) series. The double COI is related to the data gap in the *GISP* series. The coherence is high almost everywhere for timescales from 100 to almost 2500 years, except for a lacuna between 500- to 1000-year and 1500- to 2000-year periods in the late part of the time interval (after 4500 BC). Most of the spots of high coherence at short timescales can be associated with Grand minima of solar activity defined by *Usoskin et al.* [2007].

[52] The coherence between the *SP* and *AI*(*M*) series (panel h) is persistent for scales between 60–100 and 300–400 years. The high coherence at periods exceeding 600 years lies mostly within COI. Again, spots of coherence at scales shorter than 60 years correspond to Grand minima at circa 1100 AD and Spörer minimum.

3.4. Multimillennial Variations

[53] Only the longest measured ^{10}Be series, *GISP*, allows for a detailed comparison between measured and ^{14}C-based series of ^{10}Be on multimillennial timescales.

[54] As one can observe from Figure 1a, the modeled *Y*00(*M*) series reproduces centennial and millennial variability reasonably well, including, e.g., the series of peaks at approximately 3500 BC, the plateau-like excursion at around 5500 BC and three peaks of ^{10}Be concentration in the early part of the series (circa 9300, 8300 and 7500 BC). On the other hand, the reconstructed time series does not reproduce precisely all the fine features of the observed one. Also, the very long term trend does not agree, which can be observed as a mismatch of the overall level before and after the gap in the *GISP* series. Note that the modeled data lies systematically lower than the measured ^{10}Be series. A similar mismatch in the multimillennial trends between solar activity reconstructions based on ^{10}Be and ^{14}C data has been reported recently by *Vonmoos et al.* [2006]. Several reasons can be speculated for that. The ^{14}C-based reconstruction is built under a strong assumptions on the constancy of the carbon cycle parameters throughout the entire Holocene, which may not be necessarily true. Several independent proxy records suggest that the thermohaline circulation (THC) was not strictly constant in the Holocene [e.g., *Oppo et al.*, 2003; *Ellison et al.*, 2006; *Kleiven et al.*, 2008]. We note that an assumption of the THC reduced by several tens of percent in the beginning of the Holocene can potentially explain the observed difference in the long-term trends, but a detailed quantitative information about the THC variations is missing. Additional uncertainties can be related to the delayed effect of deglaciation on the ^{14}C data, and to a less extent, to possible improper modeling of the geomagnetic field.

3.5. Summary of Results

[55] From the above correlation and coherence analysis some general conclusions can be drawn.

3.5.1. Visual Inspection

[56] 1. Short- and middle-term variations of the modeled ^{10}Be series are in good agreement with the results of measurements at all the four sites.

[57] 2. A mismatch between the modeled and measured multimillennial trends is observed in the early part of the Holocene (before 7500 BC) and to a small extent prior to 4700 BC.

3.5.2. Cross-Correlation Analysis

[58] 1. Highly significant bivariate correlation exists between all pairs of the analyzed series.

[59] 2. Correlation between modeled and measured series is better than between individual measured series.

3.5.3. FFT Coherence

[60] 1. The coherence is generally low and/or insignificant for periods shorter than 50 years.

[61] 2. The coherence is high and significant for the periods above 100 years for all series except for the *SP* series.

[62] 3. The coherence of the *SP* series to other measured or modeled series is high only around a period of 100 years.

3.5.4. Wavelet Coherence

[63] 1. The coherence is always high at timescales between about 100 and 300 years. For longer series (*GISP*) the high coherence is persistent for the for scales ranging from 100 to 1000 years or even beyond.

[64] 2. The coherence is significant at short scales (<60 years) only during/around the Grand minima, when strong changes of solar activity occur quickly.

[65] 3. The seeming lack of coherence for the *SP* series is resolved when a variable phase shift is considered.

4. Discussion and Conclusions

[66] The present analysis is in agreement with earlier correlative studies [*Bard et al.*, 1997; *Vonmoos et al.*, 2006],

but provides more details and new features of the common solar signal in different cosmogenic isotope series.

[67] All measured and modeled series depict a high degree of correlation and coherence in the frequency/timescale range between roughly 100 and 1000 years. This suggest that all the series have a common variability in this frequency range. Keeping in mind that the modeled series are based on ^{14}C data, which has its own dependence on terrestrial/climate parameters, and the measured series represent antipodal locations, this points to extraterrestrial, viz. solar variability, as the common source for these coherent variations.

[68] Usually there is no coherence between the different series at scales shorter than 80–100 years. We note that coherence between modeled and measured series at short timescales is better than between individual measured data sets. This implies that although a solar signal is present also on timescales of several decades, ^{10}Be variations in polar ice are significantly affected by the local climate on these short timescales [*Lal*, 1987; *Lal and Lingenfelter*, 1991]. However, the solar signal dominates the ^{10}Be data even at short scales around periods of Grand minima of solar activity, when the driving solar activity changes greatly within a short period of time.

[69] The results for long periods (longer than a millennium) are not conclusive. On the one hand, significant coherence is observed at long timescales (about 2500 years, see Figure 4g). On the other hand, there is an unexplained discrepancy between the *GISP* and *Y*00 series in the very long term trend (Figure 1a). This discrepancy can be due to an unaccounted climate effect, most likely the not strictly valid assumption on the constancy of the ocean ventilation throughout the entire Holocene or, to a lesser extent, to possibly incorrect paleomagnetic reconstructions for the early Holocene. More detailed modeling that includes the variable carbon cycle in the earlier part of the Holocene, is beyond the scope of the present correlative study, but is planned for future studies. It is interesting to note that the difference indicates that the ^{14}C-based reconstruction of solar activity [*Solanki et al.*, 2004; *Usoskin et al.*, 2007] might be overestimated in the early part of the Holocene.

[70] The following conclusions can be drawn from the present results:

[71] 1. The ^{10}Be series, computed from ^{14}C data using a physics-based method, is in good agreement with the measured data sets, on different timescales and in different locations, confirming the validity of the used approach and the existence of the dominating common solar signal.

[72] 2. Individual ^{10}Be series are more noisy and affected by the local effects than the global ^{14}C series, which displays better agreement with the ^{10}Be data than do the individual ^{10}Be series between each other.

[73] 3. The ^{10}Be data are shown to be driven by the solar signal on the frequency/period range between roughly 100 and 1000 years.

[74] 4. Incoherent fluctuations, interpreted as local climate, dominate the ^{10}Be data on short timescales (shorter than 80–100 years), although the solar signal drives even the short-scale variability during periods of great solar activity changes (Grand minima).

[75] 5. While there is an indication that the ^{14}C-based and measured ^{10}Be series are coherent even at multimillennial timescales, the observed discrepancy in the long-term trends suggest a systematic difference in the conditions in the early Holocene, most likely due to the no entirely stable thermohaline circulation. This point calls for additional studies.

[76] Finally, we have shown that both ^{14}C- and ^{10}Be-based records are consistent with each other, both representing the dominant solar signal on a wide range of timescales and time intervals, and they form a robust basis for quantitative reconstructions of solar activity variations in the past. The solar signal gets disturbed on only short timescales of several decades or on long timescale in the early Holocene.

Appendix A: Nonparametric Random Phase Estimate of the Significance

[77] It is important to know not only the absolute value of the coherence, but also its significance, that is, the probability that it is real and not due to a random coincidence. Standard significance estimates are usually derived assuming random white noise, i.e., independent data points with Gaussian distribution. However, this is often not a case for real data, where neighboring data points are highly correlated. In such a situation, a Monte Carlo test can be applied to estimate the significance. In order to evaluate the significance of the coherence, we apply a nonparametric random phase method, as described below, suggested by *Ebisuzaki* [1997] and successfully applied in many practical studies.

[78] Let us consider two time series X and Y, whose coherence is C_{XY}. A series X is randomized (see below) to produce a new X' series, and the value of $C_{X'Y}$ is computed and compared with C_{XY}. Next, the Y series is randomized in a similar way to compute $C_{XY'}$. This procedure is repeated N times, and the number N^* is computed, which is the number of cases (within the total of N simulations) when either $C_{X'Y}$ or $C_{XY'}$ exceeds C_{XY}. Finally, the significance is defined as

$$s = N^*/N \cdot 100\%. \tag{5}$$

We note that producing the X' series by randomly shuffling the initial X series may lead to an overestimate of the significance as it destroys the serial correlation [*Usoskin et al.*, 2006d]. A more precise randomization method takes into account the serial correlation between the data points and consists of the three following steps: (1) the FFT transform of the original X series is computed; (2) the phase of the FFT series is randomized while keeping the amplitude; (3) the X' series is obtained by an inverse FFT transform of the phase-randomized series. This method, called the nonparametric random phase test, preserves the autocorrelation function of the original series.

[79] We use this method throughout the paper in order to estimate the significance, with the number of random realizations $N = 1000$.

Appendix B: Phasing Uncertainties

[80] Analysis of a time series of limited length may lead to an imprecise estimate of the phase of the formally obtained spectral components. Here we present a conservative estimate of the phasing uncertainties, being a combination of the absolute timing uncertainties of the time series and random

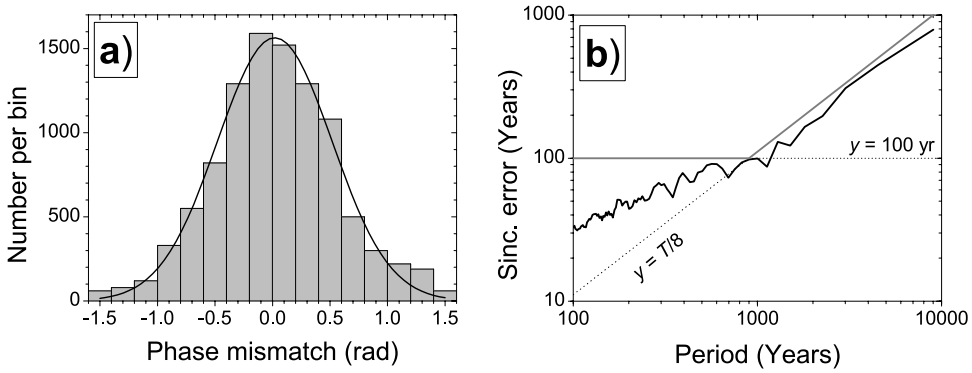

Figure 6. (a) Histogram of the phase mismatch $\Delta\psi$ at the period of ≈1000 years between the benchmark and secondary time series, together with the best fit Gaussian. (b) Phasing error $\Delta t = 2\sigma_t$ as a function of the period T (solid curve), along with the upper limit (gray broken line), used in the present study and defined as a maximum of $\Delta t = 100$ years and $\Delta t = T/8$ (equivalent of $\Delta\psi = \pi/4$).

errors related to the limited length of the series. The estimate is done using artificial series and FFT decomposition.

[81] First we produced a benchmark time series X consisting of 818 decadal points to simulate the longest *GISP* series. The series X is represented by an AR1 red noise series with the parameters (autocorrelation, variance) matching those of the *GISP* data series. Then a number of secondary time series y have been produced from the benchmark series X by adding a normally distributed noise (with zero mean and variance ξ). The value of ξ was taken equal to the variance of the *GISP* series. Next we computed the FFT decomposition of both X and y series, and the phase mismatch $\Delta\psi(T)$ between them was evaluated for each spectral component with the period T.

[82] This procedure was repeated for 100 different benchmark series X with 100 secondary series y being analyzed for each benchmark series. Thus 10,000 values of phase mismatch $\Delta\psi$ were collected for each spectral component (period T). An example of the distribution of the $\Delta\psi$ values is shown in Figure 6a for the period $T \approx 1000$ years. The distribution is nearly Gaussian (mean 0.03, $\sigma_\psi = 0.53$ rad) for long periods, but is nearly uniform for periods shorter than 200 years. The final statistical phasing errors are depicted in Figure 6b as a function of the period T. As a conservative estimate of the errors we used $\Delta\psi = 2\sigma_\psi$ Phase errors have been converted into time errors as $\Delta t = \Delta\psi \cdot T/2\pi$. A simple line of $\Delta t = T/8$, which corresponds to the fixed $\Delta\psi = \pi/4$, bounds the obtained statistical errors for periods longer than a millennium (inclined line in Figure 6b).

[83] On the other hand, the absolute dating of ^{10}Be data may be uncertain up to several decades in the early Holocene. Moreover, uncertainties of the carbon cycle model may lead to additional timing uncertainties of the ^{14}C-based series [e.g., *Damon and Peristykh*, 2004]. As a conservative upper bound we consider the absolute time accuracy to be 100 years (horizontal line in Figure 6b).

[84] Accordingly, as a conservative upper bound for the phasing errors, we use a gray curve in Figure 6b, which is defined as the maximum of statistical errors ($\pm\pi/4$ in phase) and absolute dating uncertainty (100 years).

[85] **Acknowledgments.** We acknowledge the great work done by different groups to collect and measure cosmogenic isotope data in ice cores and tree rings. When calculating wavelet coherence, we made use of a basic wavelet package in Matlab, provided by Aslak Grinsted, modified for our specific task. We acknowledge the support from the Academy of Finland and the Finnish Academy of Science and Letters (Vilho, Yrjö, and Kalle Väisälä Foundation).

[86] Zuyin Pu thanks the reviewers for their assistance in evaluating this paper.

References

Bard, E., G. M. Raisbeck, F. Yiou, and J. Jouzel (1997), Solar modulation of cosmogenic nuclide production over the last millennium: Comparison between ^{14}C and ^{10}Be records, *Earth Planet. Sci. Lett.*, *150*, 453–462, doi:10.1016/S0012-821X(97)00082-4.

Bard, E., G. M. Raisbeck, F. Yiou, and J. Jouzel (2007), Comment on "Solar activity during the last 1000 yr inferred from radionuclide records" by Muscheler et al. (2007), *Quat. Sci. Rev.*, *26*, 2301–2304, doi:10.1016/j.quascirev.2007.06.002.

Beer, J. (2000), Long-term indirect indices of solar variability, *Space Sci. Rev.*, *94*, 53–66.

Beer, J., U. Siegenthaler, H. Oeschger, G. Bonani, and R. C. Finkel (1988), Information on past solar activity and geomagnetism from Be-10 in the Camp Century ice core, *Nature*, *331*, 675–679, doi:10.1038/331675a0.

Beer, J., A. Blinov, G. Bonani, H. J. Hofmann, and R. C. Finkel (1990), Use of Be-10 in polar ice to trace the 11-year cycle of solar activity, *Nature*, *347*, 164–166, doi:10.1038/347164a0.

Belmaker, R., B. Lazar, N. Tepelyakov, M. Stein, and J. Beer (2008), *^{10}Be in Lake Lisan sediments—a proxy for production or climate?*, *Earth Planet. Sci. Lett.*, *269*, 447–456, doi:10.1016/j.epsl.2008.02.032.

Damon, P. E., and A. N. Peristykh (2004), Solar and climatic implications of the centennial and millennial periodicities in atmospheric Δ^{14}C variations, in *Solar Variability and Its Effects on Climate*, *Geophys. Monogr. Ser.*, vol. 141, edited by J. M. Pap et al., pp. 237–249, AGU, Washington D. C.

Damon, P. E., J. C. Lerman, and A. Long (1978), Temporal fluctuations of atmospheric ^{14}C: Causal factors and implications, *Ann. Rev. Earth Planet. Sci.*, *6*, 457–494, doi:10.1146/annurev.ea.06.050178.002,325.

Dorman, L. (2004), *Cosmic Rays in the Earth's Atmosphere and Underground*, Springer, New York.

Ebisuzaki, W. (1997), A method to estimate the statistical significance of a correlation when the data are serially correlated, *J. Clim.*, *10*, 2147–2153.

Ellison, C. R. W., M. R. Chapman, and I. R. Hall (2006), Surface and deep ocean interactions during the cold climate event 8200 years ago, *Science*, *312*, 1929–1932, doi:10.1126/science.1127,213.

Field, C. V., G. A. Schmidt, D. Koch, and C. Salyk (2006), Modeling production and climate-related impacts on ^{10}Be concentration in ice cores, *J. Geophys. Res.*, *111*, D15107, doi:10.1029/2005JD006410.

Finkel, R. C., and K. Nishiizumi (1997), Beryllium 10 concentrations in the Greenland Ice Sheet Project 2 ice core from 3-40 ka, *J. Geophys. Res.*, *102*, 26,699–26,706.

Fraser-Smith, A. C. (1987), Centered and eccentric geomagnetic dipoles and their poles, 1600–1985, *Rev. Geophys.*, *25*, 1–16.

Genevey, A., Y. Gallet, C. G. Constable, M. Korte, and G. Hulot (2008), ArcheoInt: An upgraded compilation of geomagnetic field intensity data for the past ten millennia and its application to the recovery of the past dipole moment, *Geochem. Geophys. Geosyst.*, *9*, Q04038, doi:10.1029/2007GC001881.

Gerber, S., F. Joos, P. Brügger, T. F. Stocker, M. E. Mann, S. Sitch, and M. Scholze (2002), Constraining temperature variations over the last millennium by comparing simulated and observed atmospheric CO_2, *Clim. Dyn.*, *20*, 281–299.

Grinsted, A., J. C. Moore, and S. Jevrejeva (2004), Application of the cross wavelet transform and wavelet coherence to geophysical time series, *Nonlinear Processes Geophys.*, *11*, 561–566.

Heikkilä, U., J. Beer, J. Jouzel, J. Feichter, and P. Kubik (2008), ^{10}Be measured in a GRIP snow pit and modeled using the ECHAM5-HAM general circulation model, *Geophys. Res. Lett.*, *35*, L05817, doi:10.1029/2007GL033067.

Horiuchi, K., A. Ohta, T. Uchida, H. Matsuzaki, Y. Shibata, and H. Motoyama (2007), Concentration of ^{10}Be in an ice core from the Dome Fuji station, Eastern Antarctica: Preliminary results from 1500 to 1810 yr AD, *Nucl. Instrum. Methods Phys. Res. Sect. B*, *259*, 584–587, doi:10.1016/j.nimb.2007.01.306.

Horiuchi, K., T. Uchida, Y. Sakamoto, A. Ohta, M. Matsuzaki, Y. Shibata, and H. Motoyama (2008), Ice core record of ^{10}Be over the past millennium from Dome Fuji, Antarctica: A new proxy record of past solar activity and a powerful tool for stratigraphic dating, *Quat. Geochronol.*, *3*, 253–261.

Hughen, K., S. Lehman, J. Southon, J. Overpeck, O. Marchal, C. Herring, and J. Turnbull (2004), ^{14}C activity and global carbon cycle changes over the past 50000 years, *Science*, *303*, 202–207.

Kay, S. (1988), *Modern Spectral Estimation: Theory and Application*, Prentice-Hall, Upper Saddle River, N. J.

Kleiven, H. F., C. Kissel, C. Laj, U. S. Ninnemann, T. O. Richter, and E. Cortijo (2008), Reduced North Atlantic deep water coeval with the glacial lake Agassiz freshwater outburst, *Science*, *319*, 60–64.

Korte, M., and C. G. Constable (2005), The geomagnetic dipole moment over the last 7000 years: New results from a global model [rapid communication], *Earth Planet. Sci. Lett.*, *236*, 348–358, doi:10.1016/j.epsl.2004.12.031.

Korte, M., and C. G. Constable (2006), Centennial to millennial geomagnetic secular variation, *Geophys. J. Int.*, *167*, 43–52.

Korte, M., and C. G. Constable (2008), Spatial and temporal resolution of millennial scale geomagnetic field models, *Adv. Space Res.*, *41*, 57–69.

Krivova, N. A., L. Balmaceda, and S. K. Solanki (2007), Reconstruction of solar total irradiance since 1700 from the surface magnetic flux, *Astron. Astrophys.*, *467*, 335–346.

Kromer, B., and M. Spurk (1998), Revision and tentative extension of the tree-ring based C-14 calibration, 9200–11855 cal BP, *Radiocarbon*, *40*, 1117–1125.

Kromer, B., S. W. Manning, P. I. Kuniholm, M. W. Newton, M. Spurk, and I. Levin (2001), Regional $^{14}CO_2$ offsets in the troposphere: Magnitude, mechanisms, and consequences, *Science*, *294*, 2529–2532.

Lal, D. (1987), ^{10}Be in polar ice: Data reflect changes in cosmic ray flux or polar meteorology, *Geophys. Res. Lett.*, *14*, 785–788.

Lal, D. (2007), Recycling of cosmogenic nuclides after their removal from the atmosphere: Special case of appreciable transport of ^{10}Be to polar regions by aeolian dust, *Earth Planet. Sci. Lett.*, *264*, 177–187, doi:10.1016/j.epsl.2007.09.030.

Lal, D., and R. Lingenfelter (1991), History of the Sun during the past 4.5 Gyr as revealed by studies of energetic solar particles recorded in extraterrestrial and terrestrial samples, in *The Sun in Time*, edited by C. P. Sonett, M. S. Giampapa, and M. S. Matthews, pp. 221–231, Univ. of Arizona Press, Tucson, Ariz.

Lal, D., A. Jull, J. T. Donahue, D. J. Burr, G. S. Deck, B. Jouzel, and J. Steig (2001), Record of cosmogenic in situ produced ^{14}C in Vostok and Taylor Dome ice samples: Implications for strong role of wind ventilation processes, *J. Geophys. Res.*, *106*, 31,933–31,942, doi:10.1029/2001JD900086.

MacMillan, S., and S. Maus (2005), International Geomagnetic Reference Field: The tenth generation, *Earth Planets Space*, *57*, 1135–1140.

McCracken, K. G. (2004), Geomagnetic and atmospheric effects upon the cosmogenic ^{10}Be observed in polar ice, *J. Geophys. Res.*, *109*, A04101, doi:10.1029/2003JA010060.

McCracken, K. G., F. B. McDonald, J. Beer, G. Raisbeck, and F. Yiou (2004), A phenomenological study of the long-term cosmic ray modulation, 850–1958 AD, *J. Geophys. Res.*, *109*, A12103, doi:10.1029/2004JA010685.

McMillan, D. G., C. G. Constable, and R. L. Parker (2004), Assessing the dipolar signal in stacked paleointensity records using a statistical error model and geodynamo simulations, *Phys. Earth Planet. Inter.*, *145*, 37–54, doi:10.1016/j.pepi.2004.02.011.

Muscheler, R., F. Joos, J. Beer, S. A. Müller, M. Vonmoos, and I. Snowball (2007), Solar activity during the last 1000 yr inferred from radionuclide records, *Quat. Sci. Rev.*, *26*, 82–97, doi:10.1016/j.quascirev.2006.07.012.

Oppo, D., J. McManus, and J. Cullen (2003), Palaeo-oceanography: Deep-water variability in the Holocene epoch, *Nature*, *422*, 277–278.

Pedro, J., T. van Ommen, M. Curran, V. Morgan, A. Smith, and A. McMorrow (2006), Evidence for climate modulation of the ^{10}Be solar activity proxy, *J. Geophys. Res.*, *111*, D21105, doi:10.1029/2005JD006764.

Raisbeck, G. M., F. Yiou, J. Jouzel, and J. R. Petit (1990), ^{10}Be and δ^2H in polar ice cores as a probe of the solar variability's influence on climate, *Philos. Trans. R. Soc. London, Ser. A*, *330*, 463–469.

Reimer, P., et al. (2004), IntCal04 terrestrial radiocarbon age calibration, 0–26 cal kyr BP, *Radiocarbon*, *46*, 1029–1058.

Siegenthaler, U., M. Heimann, and H. Oeschger (1980), ^{14}C variations caused by changes in the global carbon cycle, *Radiocarbon*, *22*, 177–191.

Snowball, I., and R. Muscheler (2007), Palaeomagnetic intensity data: An Achilles heel of solar activity reconstructions, *Holocene*, *17*, 851–859.

Solanki, S. K., I. G. Usoskin, B. Kromer, M. Schüssler, and J. Beer (2004), Unusual activity of the Sun during recent decades compared to the previous 11000 years, *Nature*, *431*, 1084–1087.

Steig, E. J., P. J. Polissar, M. Stuiver, P. M. Grootes, and R. C. Finkel (1996), Large amplitude solar modulation cycles of ^{10}Be in Antarctica: Implications for atmospheric mixing processes and interpretation of the ice core record, *Geophys. Res. Lett.*, *23*, 523–526.

Stuiver, M., and H. Pollach (1977), Discussion: Reporting of ^{14}C data, *Radiocarbon*, *19*, 355–363.

Stuiver, M., T. F. Braziunas, B. Becker, and B. Kromer (1991), Climatic, solar, oceanic, and geomagnetic influences on late-glacial and Holocene atmospheric $^{14}C/^{12}C$ change, *Quat. Res.*, *35*, 1–24, doi:10.1038/338405a0.

Stuiver, M., et al. (1998), INTCAL98 radiocarbon age calibration, 24,000–0 cal BP, *Radiocarbon*, *40*, 1041–1083.

Suess, H. (1955), Radiocarbon concentration in modern wood, *Science*, *122*, 415–417.

Tans, P., A. de Jong, and W. Mook (1979), Natural atmospheric ^{14}C variation and the Suess effect, *Nature*, *280*, 826–828.

Usoskin, I. G., and B. Kromer (2005), Reconstruction of the ^{14}C production rate from measured relative abundance, *Radiocarbon*, *47*(1), 31–37.

Usoskin, I. G., and G. A. Kovaltsov (2008), Production of cosmogenic 7Be isotope in the atmosphere: Full 3D modelling, *J. Geophys. Res.*, *113*, D12107, doi:10.1029/2007JD009725.

Usoskin, I. G., K. Mursula, S. K. Solanki, M. Schüssler, and G. A. Kovaltsov (2002), A physical reconstruction of cosmic ray intensity since 1610, *J. Geophys. Res.*, *107*(A11), 1374, doi:10.1029/2002JA009343.

Usoskin, I. G., S. K. Solanki, M. Schüssler, K. Mursula, and K. Alanko (2003), Millennium-scale sunspot number reconstruction: Evidence for an unusually active sun since the 1940s, *Phys. Rev. Lett.*, *91*(21), 211101.

Usoskin, I. G., K. Mursula, S. Solanki, M. Schüssler, and K. Alanko (2004), Reconstruction of solar activity for the last millennium using ^{10}Be data, *Astron. Astrophys.*, *413*, 745–751, doi:10.1051/0004-6361:20031,533.

Usoskin, I. G., K. Alanko-Huotari, G. A. Kovaltsov, and K. Mursula (2005), Heliospheric modulation of cosmic rays: Monthly reconstruction for 1951–2004, *J. Geophys. Res.*, *110*, A12108, doi:10.1029/2005JA011250.

Usoskin, I. G., S. K. Solanki, and M. Korte (2006a), Solar activity reconstructed over the last 7000 years: The influence of geomagnetic field changes, *Geophys. Res. Lett.*, *33*, L08103, doi:10.1029/2006GL025921.

Usoskin, I. G., S. K. Solanki, G. A. Kovaltsov, J. Beer, and B. Kromer (2006b), Solar proton events in cosmogenic isotope data, *Geophys. Res. Lett.*, *33*, L08107, doi:10.1029/2006GL026059.

Usoskin, I. G., S. K. Solanki, C. Taricco, N. Bhandari, and G. A. Kovaltsov (2006c), Long-term solar activity reconstructions: Direct test by cosmogenic 44Ti in meteorites, *Astron. Astrophys.*, *457*, L25–L28, doi:10.1051/0004-6361:20065,803.

Usoskin, I. G., M. Voiculescu, G. A. Kovaltsov, and K. Mursula (2006d), Correlation between clouds at different altitudes and solar activity: Fact or artifact?, *J. Atmos. Sol. Terr. Phys.*, *68*, 2164–2172, doi:10.1016/j.jastp.2006.08.005.

Usoskin, I. G., S. K. Solanki, and G. A. Kovaltsov (2007), Grand minima and maxima of solar activity: New observational constraints, *Astron. Astrophys.*, *471*, 301–309.

Usoskin, I. G., M. Korte, and G. A. Kovaltsov (2008), Role of centennial geomagnetic changes in local atmospheric ionization, *Geophys. Res. Lett.*, *35*, L05811, doi:10.1029/2007GL033040.

Vinther, B. M., et al. (2006), A synchronized dating of three Greenland ice cores throughout the Holocene, *J. Geophys. Res.*, *111*, D13102, doi:10.1029/2005JD006921.

Vonmoos, M., J. Beer, and R. Muscheler (2006), Large variations in Holocene solar activity: Constraints from ^{10}Be in the Greenland Ice Core Project ice core, *J. Geophys. Res.*, *111*, A10105, doi:10.1029/2005JA011500.

Yang, S., H. Odah, and J. Shaw (2000), Variations in the geomagnetic dipole moment over the last 12,000 years, *Geophys. J. Int.*, *140*, 158–162.

E. Bard, Collége de France, Université Paul-Cézanne Aix-Marseille 3, Europole de l'Arbois BP80, F-13545 Aix-en-Provence CEDEX 4, France.

K. Horiuchi, Faculty of Science and Technology, Hirosaki University, 3 Bunkyo-cho, Hirosaki, Aomori 036-8561, Japan.

G. A. Kovaltsov, Ioffe Physical-Technical Institute, Politekhnicheskaya 26, RU-194021 St. Petersburg, Russia.

S. Solanki, Max-Planck Institute for Solar System Research, Max-Planck-Str. 2, D-37191 Katlenburg-Lindau, Germany.

I. G. Usoskin, Sodankylä Geophysical Observatory, University of Oulu, P.O. Box 3000, FIN-90014 Oulu, Finland. (ilya.usoskin@oulu.fi)